J Mater Sci (2021) 56:3011–3023

Chemical routes to materials

Branched nanosheets-interlaced structure of Co^{2+}/Co^{3+}-doped $Ni(OH)_2$ originating from $Ni_3(NO_3)_2(OH)_4$ template with significantly boosted electrochemical performance

Jing Wang[1], Jing Li[1], Yuanyuan Liu[1], Meiri Wang[1], and Hongtao Cui[1,*]

[1] School of Chemistry and Chemical Engineering, Yantai University, Yantai 264005, China

Received: 15 August 2020
Accepted: 13 October 2020
Published online: 23 October 2020

© Springer Science+Business Media, LLC, part of Springer Nature 2020

ABSTRACT

The cycling stability of electrode materials is a key for Faraday supercapacitors (FSs), especially the structure-unstable $Ni(OH)_2$. There exist various strategies for stabilizing the structure of $Ni(OH)_2$ such as cobalt ions doping and mechanical support from substrate. However, these strategies have their own disadvantages. On the other hand, the combination of two or more strategies has the serious issues in materials synthesis. In this work, a branched nanosheets-interlaced structure of Co^{2+}/Co^{3+}-doped $Ni(OH)_2$ is built by a method of precursor template, which effectively applies two strategies including ions doping and self-supportive structure. Due to the synergistic contribution of these two strategies, the cycling stability of as-prepared material is significantly enhanced. This material also presents excellent high-rate capacity, and the as-assembled asymmetric supercapacitors (ASCs) show both high energy and power densities. These results prove that the effective combination of ions doping and self-supportive structure strategies is a promising route for the preparation of $Ni(OH)_2$-based electrode materials with high performance.

Introduction

Nickel-based materials are a category of intensively investigated battery-type electrode materials for application in FSs. These materials include $Ni(OH)_2$, nickel-based double-layered hydroxides, nickel-based sulfide, and selenides [1–4]. $Ni(OH)_2$ has been considered as an important electrode material for application in FSs because of its high theoretical capacity [5]. Although $Ni(OH)_2$ has satisfied electrochemical performance in alkaline batteries, it presents poor high-rate performance and cycling stability when it is transplanted directly to FSs. It is widely accepted that the poor performance of $Ni(OH)_2$ in FSs originates from its low ionic/electronic conductivities

Handling Editor: Yaroslava Yingling.

Address correspondence to E-mail: htcui@ytu.edu.cn

https://doi.org/10.1007/s10853-020-05446-0

and low structural instability [6]. To solve these two issues, nanoengineering the structure of $Ni(OH)_2$ has been the only feasible strategy so far [7, 8].

During the charge–discharge cycles, the layer-structured $Ni(OH)_2$ undergoes the following reversible redox reaction in alkaline electrolyte solution: $Ni(OH)_2 + OH^- \leftrightarrow NiOOH + H_2O + e^-$ [9]. The cycling phase transformation between $Ni(OH)_2$ and NiOOH results in the cycling volumetric swell and shrink due to their different densities. Based on the theoretical density data [10, 11], it is known that the volumetric change fraction of material because of the phase transformation between $Ni(OH)_2$ and NiOOH is 24.0%. This implies that the phase transformation can significantly affect the stability of material. It is also known that the electronic conductivity of NiOOH is more than five orders of magnitude higher than that of $Ni(OH)_2$. In other words, the electronic conductivity of $Ni(OH)_2$-based electrode materials switches between low and high conductivities corresponding to the switch of discharge and charge stages. Due to the slow diffusion rate of OH^- ions in solid phase, the materials cannot be fully charged or discharged at high rate [12]. As a result, the low-conductivity $Ni(OH)_2$ ever exists in material throughout the charge–discharge cycles, leading to the low electronic conductivity of materials along with poor high-rate performance. Therefore, shortening the diffusion path of OH^- ions by reducing the layers of $Ni(OH)_2$ has become the only choice to increase the ionic and electronic conductivities of materials. The issue arising from this practice is that the particulate-like $Ni(OH)_2$ aggregates composed of flexible thin nanosheets are not capable to resist the stress originating from the cycling volume change of materials [13]. The capacity of materials would rapidly decay with the microstructure collapse of aggregates. Therefore, there should be a comprise between the thickness and structural stability of nanosheets. Namely, the nanosheets should have an appropriate thickness in order to improve the cycling stability of $Ni(OH)_2$ and meanwhile have the accepted diffusion path.

It should be pointed out that increasing the thickness of nanosheets is not a well-accepted strategy due to its limited effect on the cycling stability of $Ni(OH)_2$. There exist two other effective strategies for this aim: (1) growing $Ni(OH)_2$ on the skeleton surface of current collectors such as nickel foam [14–16] and carbon cloth [17, 18] to buffer the electrochemical stress and (2) doping cobalt ions in $Ni(OH)_2$ to enhance its structural stability. In the first strategy, the $Ni(OH)_2$ nanosheets have to be organized to a surface-clung 2D blanket-like collective structure to keep low series resistance in electrodes. The issue arising from this strategy is the low materials loading in electrodes due to the intrinsic low surface area of current collectors [1, 19]. In the second strategy, the doped cobalt ions mitigate the Jahn–Teller effect of nickel ions and thus stabilize the crystallographic octahedral framework of $Ni(OH)_2$ [20]. This strategy is effective to a certain degree; however, it still cannot satisfactorily promote the cycling stability of $Ni(OH)_2$. In a recently published article, we proposed a strategy of self-supportive structure to promote the cycling stability of $Ni(OH)_2$ [21]. We built a branched thin nanosheets-interlaced structure of $Ni(OH)_2$ through the isostructured $Ni_3(NO_3)_2(OH)_4$ template. This nanosheets self-supportive structure provides additional mechanical stability, thus leading to the promoted cycling stability of $Ni(OH)_2$. However, it is pity that the cycling stability of $Ni(OH)_2$ in this work is still not satisfied (70% capacity retention after 5000 charge–discharge cycles).

Herein, we believe that synergistic application of cobalt ions doping and nanosheets self-supportive structure can result in the cycling stability-satisfied $Ni(OH)_2$. However, the cobalt ions-doped $Ni(OH)_2$ synthesized by the frequently used precipitation [22] and hydrothermal methods [1, 23, 24] present nanosheets-twined structure without strong interaction between nanosheets in most cases. Consequently, these as-produced cobalt ions-doped $Ni(OH)_2$ cannot present satisfied cycling stability. In this work, we synthesized cobalt ions-doped $Ni_3(NO_3)_2(OH)_4$ with branched nanosheets-interlaced structure by an ions-exchange method. During the following treatment in alkaline solution, the produced cobalt ions-doped $Ni(OH)_2$ inherited the nanostructure of doped $Ni_3(NO_3)_2(OH)_4$ intactly. Due to the nanosheets self-supportive structure, the $Ni(OH)_2$ and the as-assembled ASCs presented satisfied cycling stability besides high electrochemical performance.

Experimental

Nickel nitrate hexahydrate ($Ni(NO_3)_2{\cdot}6H_2O$, ≥ 98%), nickel chloride hexahydrate ($NiCl_2{\cdot}6H_2O$, ≥ 98%), cobalt nitrate hexahydrate ($Co(NO_3)_2{\cdot}6H_2O$, ≥ 98%),

propylene oxide (C_3H_6O, ≥ 99%), potassium hydroxide (KOH, ≥ 99%), and ethanol (≥ 99.5%) were purchased from Shanghai Aladdin Bio-Chem Technology Co., LTD, and used as received.

Preparation of $Ni_3(NO_3)_2(OH)_4$

0.0135 mol $Ni(NO_3)_2{\cdot}6H_2O$ was added to a 150 mL beaker containing 90 mL ethanol under the stirring of a stir bar, forming a transparent 0.15 M nickel salt solution. After the addition of 10 mL propylene oxide, the beaker was heated in a 70 °C water bath under magnetic stirring for 60 min and then naturally cooled to room temperature. The produced precipitate was separated by vacuum filtration and washed by distilled water and ethanol. The isolated precipitate was heated at 60 °C in an oven until dry powder of $Ni_3(NO_3)_2(OH)_4$ was obtained.

Preparation of Co^{2+}/Co^{3+}-doped $Ni_3(NO_3)_2(OH)_4$

A transparent 0.1 M cobalt salt solution was formed by dissolving 0.004 mol $Co(NO_3)_2{\cdot}6H_2O$ in 40 mL distilled water under magnetic stirring in a 50 mL beaker. Then, the $Ni_3(NO_3)_2(OH)_4$ powder was dispersed in this solution by ultrasonification for 10 min, forming a suspension. The suspension in beaker was transferred into a double-walled vessel with an inner liner and a cover made of Teflon perfluoroalkoxy (PFA) polymer resin and an outer high strength sleeve. The sealed vessel was directly heated to 130 °C by a XH-800G microwave-heated reaction system (Beijing Xianghu Science and Technology Development Co., Ltd.) at a power of 700 W. The reaction in the vessel was carried out at 130 °C for 30 min with pressure of slightly less than 1 MPa.

After the reaction, the precipitates were separated by vacuum filtration, washed with distilled water and ethanol, and then dried at 60 °C in an oven.

Characterization

The structure of samples was characterized by a Rigaku Smart Lab III diffractometer (XRD) using Cu Kα radiation (λ = 1.5406 Å) and a Shimadzu IRAffinity-1S spectrometer (FTIR) using KBr pellet technique. The N_2 adsorption/desorption isotherms of samples were measured by an ASAP-2010 surface area analyzer. The morphology of samples was observed by a JEOL JSM-7900F thermal field emission scanning electron microscope (FE-SEM). The element analysis on samples was carried out on an ESCALAB Xi + X-ray photoelectron spectrometer (XPS) and an Oxford Ultim Extreme energy-dispersive spectrometer (EDS). The composition of samples was analyzed by a Thermo IRIS Intrepid II XSP inductively coupled plasma atomic emission spectrometer (ICP-AES).

Electrochemical measurements

A three-electrode system includes a working electrode, a reference electrode of Hg/HgO, and a platinum plate counter electrode. This system was attached to an IVIUMSTAT electrochemical workstation and used to measure the electrochemical properties of materials in a 3 M KOH aqueous solution. A 1 × 1 × 0.15 cm nickel foam was homogeneously coated with a mixture layer of 80 wt% electro-active materials and 20 wt% acetylene black by compression at 10 Mpa. The coated nickel foam was then used as a working electrode for electrochemical measurement. The measurements include cyclic voltammetry (CV), galvanostatic charge–discharge (GCD), and electrochemical impedance spectroscopy (EIS). The cycling life of materials was tested by a LANHE CT2001A batteries testing system in the three-electrode system. Before electrochemical measurements, the working electrode was electro-activated by 100 cycles of cyclic voltammetry at scan rate of 100 mV s^{-1} within the potential window of 0–0.55 V.

The specific capacity (C g^{-1}) of electrode materials in three-electrode configuration was calculated from GCD discharge curves with Eq. (1):

$$C = \frac{It}{m} \tag{1}$$

where I, t, and m are designated as discharge current (A), discharge time (s), and loading mass (g) of active material, respectively.

The specific capacitance (F g^{-1}) of electrode materials in three-electrode configuration was calculated from GCD discharge curves with Eq. (2):

$$C = \frac{It}{mV} \tag{2}$$

where I, t, m, and V are discharge current (A), discharge time (s), loading mass (g), and potential range (V), respectively.

The ASCs include activated carbon (AC) as negative electrode, electro-active material as positive electrode, and a nonwoven diaphragm. The ASCs were assembled in a CR2016-type coin cell using 3 M KOH solution as electrolyte. The mass of positive and negative electrodes was balanced with Eqs. (3):

$$\frac{m_-}{m_+} = \frac{C_- v_-}{C_+} \tag{3}$$

where m_- and m_+ are, respectively, the mass (g) of negative and positive electrodes, C_- is the specific capacitance (F g^{-1}) of negative electrode, C_+ is the specific capacity (C g^{-1}) of positive electrode, and v_- is the voltage range (V) of negative electrode.

The specific capacity (C g^{-1}), energy density (Wh kg^{-1}), and power density (W kg^{-1}) of ASCs were calculated from GCD curves with Eqs. (4–6):

Specific capacity:

$$C = \frac{IT}{MV} \tag{4}$$

Energy density:

$$E = \frac{1}{3.6}\frac{I\int vdT}{M} \tag{5}$$

Power density:

$$P = \frac{3600E}{T} \tag{6}$$

where V, I, M, and T are operating voltage window (V), discharge current (A), total loading mass (g) of both negative and positive electrodes, and discharge time (s), respectively.

Results and discussion

As illustrated in Fig. 1, the branched nanosheets-interlaced structure of Co^{2+}/Co^{3+}-doped $Ni(OH)_2$ was built through a sequent three-step process: (1) building the branched nanosheets-interlaced structure of $Ni_3(NO_3)_2(OH)_4$ by epoxide precipitation reaction; (2) doping Co^{2+}/Co^{3+} ions in $Ni_3(NO_3)_2(OH)_4$ by ions exchange at microwave-assisted hydrothermal conditions, while keeping the original structure of $Ni_3(NO_3)_2(OH)_4$; (3) in situ transformation of Co^{2+}/Co^{3+}-doped $Ni_3(NO_3)_2(OH)_4$ into Co^{2+}/Co^{3+}-doped $Ni(OH)_2$ with the branched nanosheets-interlaced structure in alkaline electrolyte solution.

The $Ni_3(NO_3)_2(OH)_4$ was produced through the ring-opening reaction of epoxide in ethanolic solution [25]. The XRD pattern in Fig. 2a indicates that the produced sample has the typical crystallographic structure of $Ni_3(NO_3)_2(OH)_4$ (JCPDS 22–0752). We tried to dope cobalt ions in $Ni_3(NO_3)_2(OH)_4$ at atmospheric condition; however, the ions doping was not successful no matter how we controlled temperature and ions concentration. Therefore, we tried to dope cobalt ions in $Ni_3(NO_3)_2(OH)_4$ at microwave-assisted hydrothermal condition. The XRD pattern in Fig. 2a shows that the doped sample still keeps the structure of $Ni_3(NO_3)_2(OH)_4$ but with much lowered crystallinity. In Table 1, the structure data derived from the XRD data are given to prove the effect of cobalt ions doping on the structure of $Ni_3(NO_3)_2(OH)_4$. This table shows that the structure data of doped sample including d-spacing, crystallize size, and lattice parameters are quite different from $Ni_3(NO_3)_2(OH)_4$. This result can be an important evidence of successful cobalt ions doping in the lattice. In the XPS survey scan spectra (Fig. 2b), $Ni_3(NO_3)_2(OH)_4$ presents the peaks of Ni 2p, Ni 3p, Ni 3 s, N 1 s, and C1s besides the Ni and O Auger lines, while the cobalt ions-doped $Ni_3(NO_3)_2(OH)_4$ shows the additional peak of Co 2p. In the fitted Ni 2p spectra (Fig. 2c), $Ni_3(NO_3)_2(OH)_4$ presents the two peaks at 855 and 872.7 eV ascribed to Ni^{2+}, and the two peaks at 856.6 and 874.0 eV assigned to Ni^{3+} [23, 24, 26]. Meanwhile, it is observed that the cobalt ions-doped $Ni_3(NO_3)_2(OH)_4$ has only the two peaks at 855.3 and 873.2 eV belonging to Ni^{2+} with slight blueshift as compared with $Ni_3(NO_3)_2(OH)_4$. This binding energy blueshift of Ni^{2+} can be attributed to the doping of cobalt ions. The result of XPS Ni 2p proves that the doped cobalt ions depress the oxidization of some Ni^{2+} ions to Ni^{3+} ions. This result also implies the successful doping of cobalt ions in the lattice of $Ni_3(NO_3)_2(OH)_4$ beside the XRD results [27]. In the fitted Co 2p spectrum of Fig. 2d, the cobalt ions-doped $Ni_3(NO_3)_2(OH)_4$ exhibits the two peaks at 781.3 and 797.6 eV ascribed to Co^{2+} and the other two peaks at 780.2 and 796.1 eV assigned to Co^{3+}. To further confirm whether the cobalt ions are adsorbed on the surface or doped in the lattice, we etched the doped $Ni_3(NO_3)_2(OH)_4$ by ion gun before the XPS characterization to expose a new surface approximately 10 nm lower than the original sample. The Ni 2p spectrum of etched sample in Fig. S1a shows the same profile to the original sample, while its Co 2p

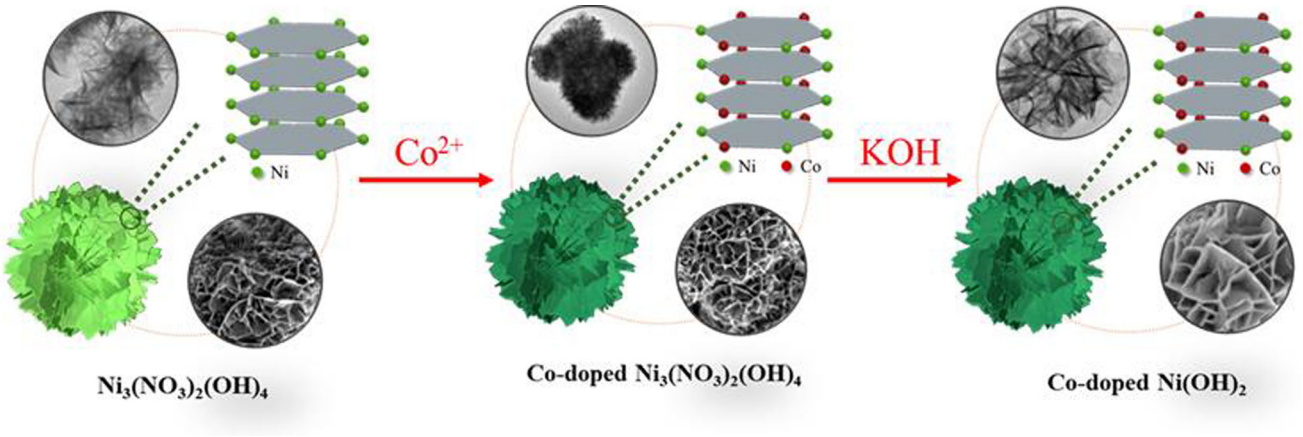

Figure 1 Schematic illustration for the preparation of Co^{2+}/Co^{3+}-doped $Ni(OH)_2$ with the branched nanosheets-interlaced structure.

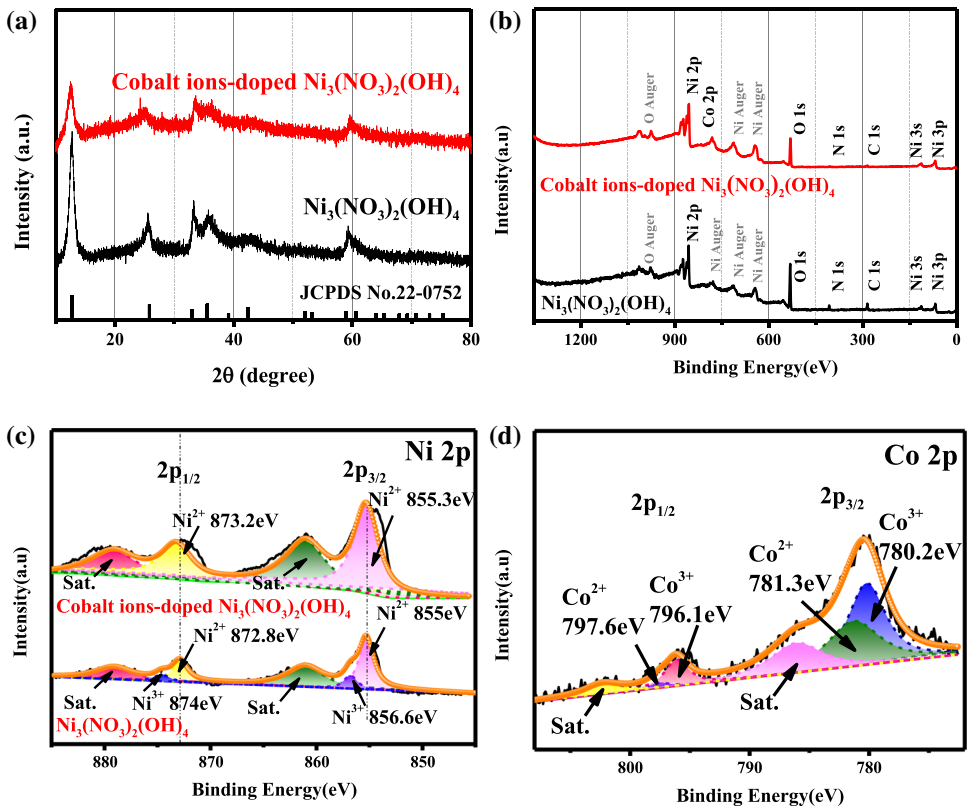

Figure 2 (**a**) XRD patterns, (**b**) XPS survey spectra, and (**c**) XPS Ni 2p spectra of $Ni_3(NO_3)_2(OH)_4$ and cobalt ions-doped $Ni_3(NO_3)_2(OH)_4$; (**d**) XPS Co 2p of cobalt ions-doped $Ni_3(NO_3)_2(OH)_4$.

Table 1 The d-spacing, crystallite size, and lattice parameters of samples

Sample	d-spacing	Crystallite size	Lattice parameters		
			a/(Å)	b/(Å)	c/(Å)
$Ni_3(NO_3)_2(OH)_4$	6.97	11.17 nm	3.11812	3.11812	6.92423
Cobalt ions-doped $Ni_3(NO_3)_2(OH)_4$	7.06	9.49 nm	3.12941	3.12941	6.89523

spectrum indicates the slight blueshift as compared with the original sample. Herein, the existence of cobalt ions in the etched sample proven by XPS further confirms the doping of cobalt ions instead of surface adsorption.

FE-SEM and TEM were used to characterize the morphologies of $Ni_3(NO_3)_2(OH)_4$ and Co^{2+}/Co^{3+}-doped $Ni_3(NO_3)_2(OH)_4$. It is observed in the images of Fig. 3a-d that the $Ni_3(NO_3)_2(OH)_4$ presents the branched thin nanosheets-interlaced flower-like nanostructure, suggesting the strong bonding between nanosheets. Based on the electrochemical mechanism of FSs, it can be inferred that this structure has multiple functions: (1) rich electro-active sites; (2) 2D nanosheets with short diffusion path for electrolyte ions; (3) porous channels for the facile transfer of electrolyte ions into and out of material; and (4) self-supportive nanosheets with additional mechanical stability. In the images of Fig. 3e-h, Co^{2+}/Co^{3+}-doped $Ni_3(NO_3)_2(OH)_4$ exhibits the exactly same morphology to $Ni_3(NO_3)_2(OH)_4$, implying that the cobalt ions doping has no influence on morphology. The EDS elemental mapping result in Fig. 3i shows that the two elements of Ni and Co are homogeneously distributed in the sample. The EDS elemental analysis result indicates that the atomic ratio of Co to Ni is 1:5 in this sample, while the ICP analysis result shows that the atomic ratio of Co to Ni is 1:7 in the same sample. It is known that the ICP analysis has high accuracy on the analysis of elemental composition. Therefore, we consider that the atomic ratio of Co to Ni in Co^{2+}/Co^{3+}-doped $Ni_3(NO_3)_2(OH)_4$ should be 1:7 instead of 1:5.

The N_2 adsorption/desorption measurements on $Ni_3(NO_3)_2(OH)_4$ and Co^{2+}/Co^{3+}-doped $Ni_3(NO_3)_2(OH)_4$ were performed to explore their surface properties. As shown in Fig. 3j, both samples show the type IV adsorption/desorption isotherms, suggesting their mesoporous properties. The specific surface areas of $Ni_3(NO_3)_2(OH)_4$ and Co-doped $Ni_3(NO_3)_2(OH)_4$ calculated by Brunauer–Emmett–Teller method (BET) are 161.6 $m^2\ g^{-1}$ and 134.1 $m^2\ g^{-1}$, respectively. The pore-size distribution curves in Fig. 3k

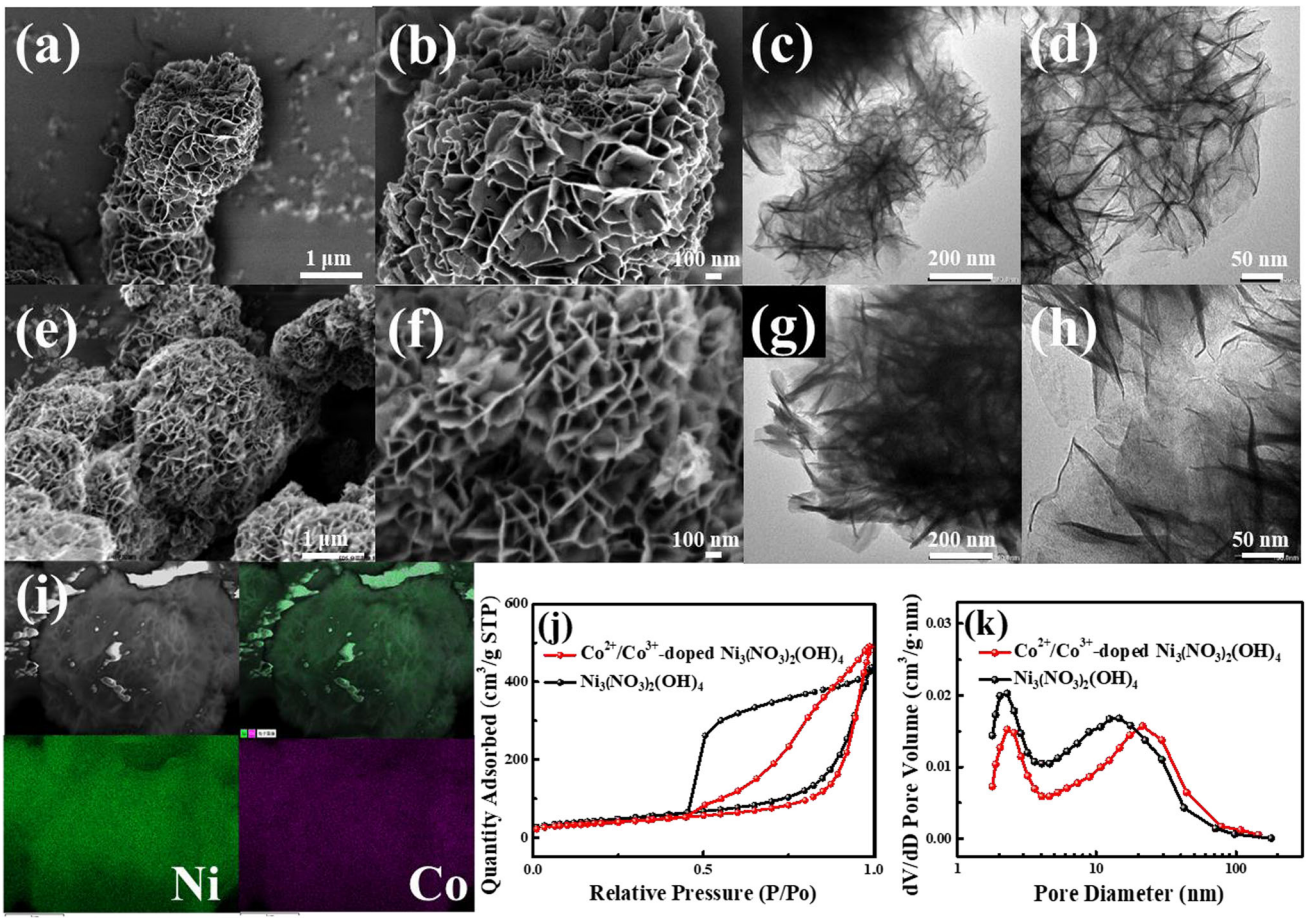

Figure 3 **a**, **b** FE-SEM and **c**, **d** TEM images of $Ni_3(NO_3)_2(OH)_4$; **e**, **f** FE-SEM images and **g**, **h** TEM images of Co^{2+}/Co^{3+}-doped $Ni_3(NO_3)_2(OH)_4$; **i** elemental mapping of Co^{2+}/Co^{3+}-doped $Ni_3(NO_3)_2(OH)_4$; **j** N_2 adsorption/desorption isotherms; and **k** pore-size distribution of $Ni_3(NO_3)_2(OH)_4$ and Co^{2+}/Co^{3+}-doped $Ni_3(NO_3)_2(OH)_4$.

derived from isotherms indicate that the two samples have the same profile with concentrated pore-size distribution below 100 nm. The surface characterization results demonstrate that cobalt ions doping just decreases the surface area of doped sample slightly and does not change its pore structure.

The Co^{2+}/Co^{3+}-doped $Ni_3(NO_3)_2(OH)_4$ was directly used as electrode material to assemble working electrode. It is known in our previous work [21] that the $Ni_3(NO_3)_2(OH)_4$ is transformed into α- and β-type structural motifs interstratified $Ni(OH)_2$ (α/β-$Ni(OH)_2$) in KOH solution before electrochemical measurement. Therefore, we also characterized the structure of cobalt ions-doped sample soaked in KOH solution before electrochemical measurement. Its XRD pattern in Fig. 4a indicates that the sample has the mixed phases of α-$Ni(OH)_2$ and β-$Ni(OH)_2$. The FTIR spectra in Fig. S2 show that both $Ni_3(NO_3)_2(OH)_4$ and Co^{2+}/Co^{3+}-doped $Ni_3(NO_3)_2(OH)_4$ possess the typical sharp peak of structural NO^{3-} ions at 1384 cm^{-1} and the wide peak of hydrogen-bonded hydroxyl belonging to $Ni_3(NO_3)_2(OH)_4$ and adsorbed water around 3510 cm^{-1}. On the other hand, the FTIR spectra in Fig. 4b and Fig. S2 for these two samples treated in KOH solution show the coexistence of the characteristic signals of α-$Ni(OH)_2$ and β-$Ni(OH)_2$: (1) The widened peak at 1384 cm^{-1} is assigned to the vibration band of intercalated NO^{3-} ions in the interlayer space of α-$Ni(OH)_2$ [28]; the peak at 3640 cm^{-1} is assigned to the characteristic v(OH) stretching vibration band of free hydroxyl groups in β-$Ni(OH)_2$ [9]. This result demonstrates that this sample also has the structure of α/β-$Ni(OH)_2$. Hall et al. pointed out that the α-$Ni(OH)_2$ and β-$Ni(OH)_2$ domains coexist within a single crystal for α/β-$Ni(OH)_2$ [9]. Therefore, it is reasonable to infer in this work that only the Co^{2+} ions are doped in the β-$Ni(OH)_2$ motif of α/β-$Ni(OH)_2$, and the Co^{2+} and Co^{3+} ions are co-doped in the α-$Ni(OH)_2$ motif similar to the situation in Ni-Co LDH.

To investigate the effect of phase transformation, the surface properties and morphology of Co^{2+}/Co^{3+}-doped $Ni(OH)_2$ were characterized. As shown in Fig. 4c, this sample presents the type IV N_2 adsorption and desorption isotherms. Its BET specific surface area is about 107.4 $m^2\ g^{-1}$, while its pore-size distribution curve in the inset of Fig. 4c indicates the similar pore structure to its precursor. In the FE-SEM and TEM images of Fig. 4d-g, the Co^{2+}/Co^{3+}-doped $Ni(OH)_2$ presents an almost same structure to its precursor. The EDS elemental mapping result in Fig. 4h shows that the Ni and Co elements are homogeneously distributed in this sample. These results suggest that the Co^{2+}/Co^{3+}-doped $Ni(OH)_2$ inherits the structure of its precursor although its specific surface area is reduced in a certain degree.

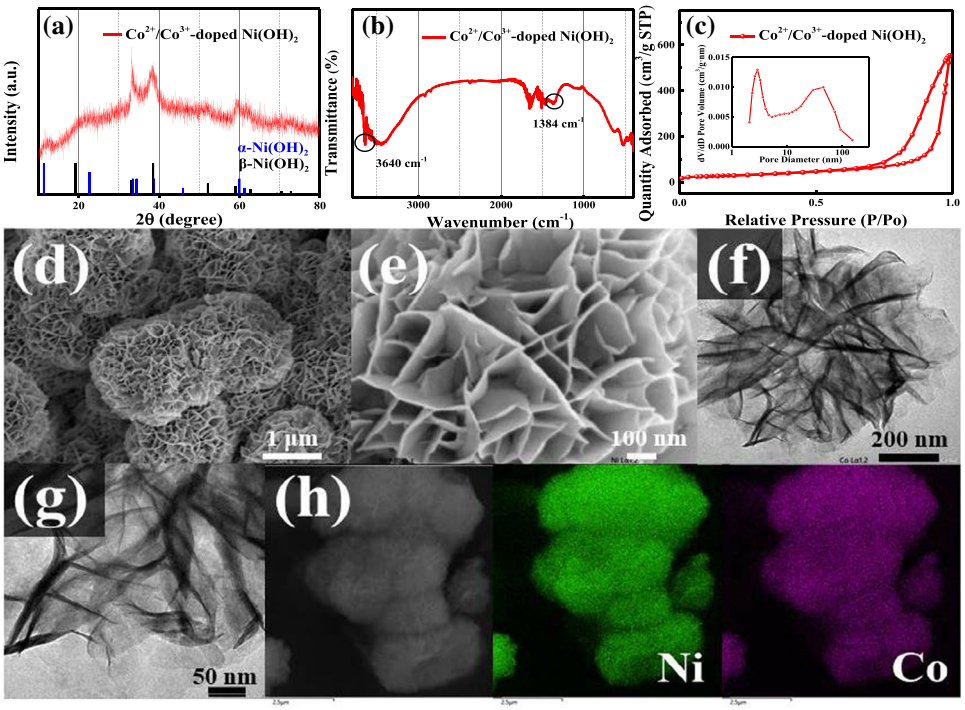

Figure 4 (a) XRD pattern, (b) FTIR spectrum, (c) N_2 adsorption and desorption isotherms, pore-size distribution curves inset, (d, e) FE-SEM images, (f, g) TEM images, and (h) EDS element mapping for the sample obtained after the soaking of Co^{2+}/Co^{3+}-doped $Ni_3(NO_3)_2(OH)_4$ in KOH solution.

Theoretically, the Co^{2+}/Co^{3+}-doped $Ni(OH)_2$ has the nearly ideal structure for its electrochemical performance. It should present high specific capacity and high cycling stability. Therefore, we carried out electrochemical measurement on this sample to confirm our inference. At the same time, we also measured the electrochemical properties of the $Ni(OH)_2$ that was transformed from $Ni_3(NO_3)_2(OH)_4$ to compare with Co^{2+}/Co^{3+}-doped $Ni(OH)_2$. In Fig. 5a, a pair of nearly symmetrical redox peaks appear in the CV curves of both samples at scan rate of 5 mV s^{-1}, corresponding to their reversible redox reactions. It is observed in this figure that the potential difference (133 mV) of Co^{2+}/Co^{3+}-doped $Ni(OH)_2$ between its redox peaks is much less than that of $Ni(OH)_2$ (203 mV), suggesting its higher reaction reversibility. In the GCD curves of Fig. 5b, the Co^{2+}/Co^{3+}-doped $Ni(OH)_2$ shows much longer charge–discharge duration at high current density of 33.0 A g^{-1} than $Ni(OH)_2$.

In Fig. 5c, the specific capacities of both samples at different current densities were calculated from their discharge curves. This figure shows that the Co^{2+}/Co^{3+}-doped $Ni(OH)_2$ has specific capacities of 999.0, 952.9, 837.8, 782.4, 624.1, 531, and 428.5 C g^{-1} at the respective current densities of 2.0, 4.1, 14.3, 20.5, 41.0, 61.7, and 94.3 A g^{-1}, much higher than those of $Ni(OH)_2$ at corresponding current densities. The Co^{2+}/Co^{3+}-doped $Ni(OH)_2$ has very excellent high-rate capacity. It still keeps a high capacity retention of 43% at a high current density of 94.3 A g^{-1}, while $Ni(OH)_2$ just presents a very low value of 7% at the current density of 43.4 A g^{-1}. To confirm the high-rate advantage of Co^{2+}/Co^{3+}-doped $Ni(OH)_2$, we translate the specific capacity (C g^{-1}) to specific capacitance (F g^{-1}) in Fig. 5d to compare with the cobalt ions-doped $Ni(OH)_2$ prepared in recently published works. This figure demonstrates that Co^{2+}/Co^{3+}-doped $Ni(OH)_2$ is much superior in high-rate capacity to other works [8, 17, 23–26].

In Fig. 5e, the Nyquist plots of Co^{2+}/Co^{3+}-doped $Ni(OH)_2$ and $Ni(OH)_2$ derived from their EIS are fitted by software Zview using the equivalent circuit shown in inset. The elements of equivalent circuit include series resistance (R_{st}), charge transfer resistance (R_{ct}), Warburg impedance (W), and constant phase element (CPE). In this figure, the almost vanished semicircles in high-frequency region for both samples indicate their low R_{ct}, suggesting their high redox reaction reactivity. The larger slope of straight

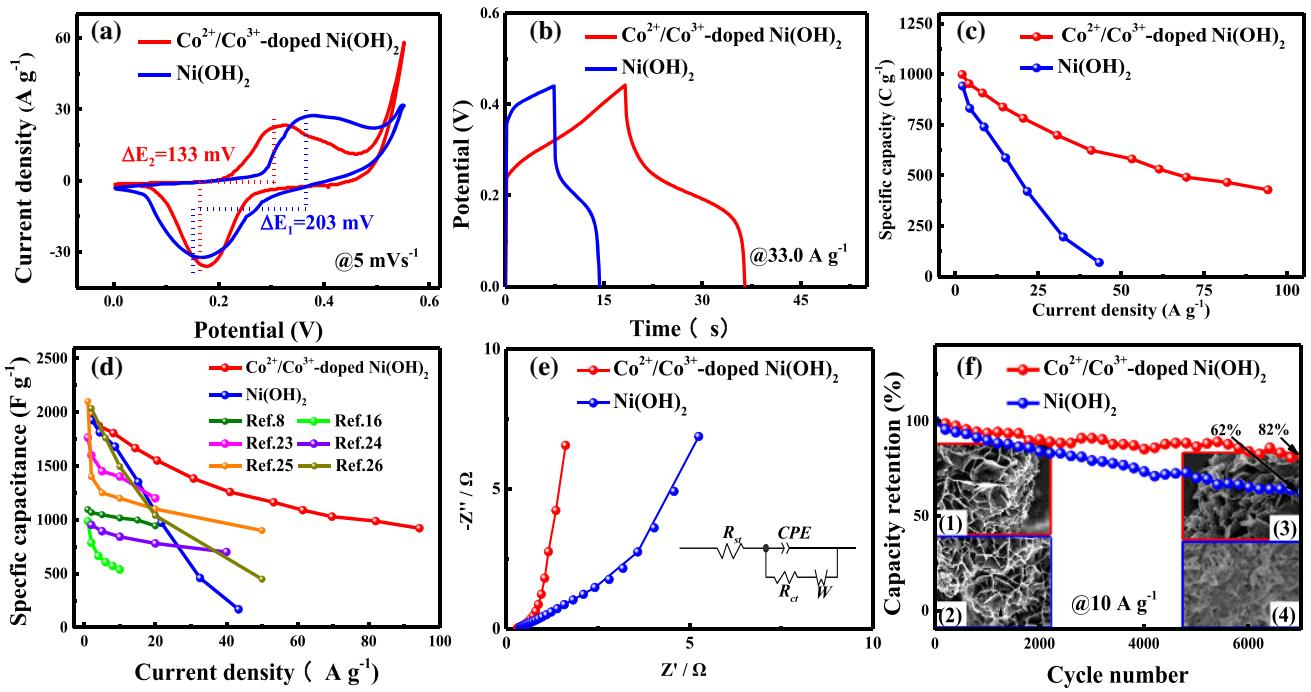

Figure 5 (a) CV curves at scan rate of 5 mV s^{-1}, (b) GCD curves at current density of 33.0 A g^{-1}, (c) curves of specific capacity vs. current density, (d) capacitance comparison, (e) Nyquist plots, and (f) cycling stability at 10.0 A g^{-1} of Co^{2+}/Co^{3+}-doped $Ni(OH)_2$ and $Ni(OH)_2$.

line of Co^{2+}/Co^{3+}-doped $Ni(OH)_2$ than $Ni(OH)_2$ in low-frequency region indicates its lower *W*, demonstrating its more facile transfer of electrolyte ions inside pores. This result is a proof for the excellent high-rate capacity of Co^{2+}/Co^{3+}-doped $Ni(OH)_2$. In the cycling stability test result of Fig. 5f, the Co^{2+}/Co^{3+}-doped $Ni(OH)_2$ shows much higher stability than $Ni(OH)_2$ at current density of 10.0 A g^{-1}. After 7000 charge–discharge cycles, the Co^{2+}/Co^{3+}-doped $Ni(OH)_2$ exhibits a high capacity retention of 82%, while $Ni(OH)_2$ shows the much lower capacity retention of 62%. As shown in the inset images of Fig. 5f, the Co^{2+}/Co^{3+}-doped $Ni(OH)_2$ remains most of its original pore structure after 7000 cycles. On the contrary, most of the pore structure of $Ni(OH)_2$ collapses. This result demonstrates that the doped cobalt ions do enhance the structural stability of $Ni(OH)_2$. To confirm the advantages of Co^{2+}/Co^{3+}-doped $Ni(OH)_2$, its cycling stability is compared in Table 2 with other cobalt ions-doped $Ni(OH)_2$ prepared in recent typical works [1, 19, 22, 29–38]. It is shown in this table that most works adopted the two strategies mentioned in introduction to promote the cycling stability of $Ni(OH)_2$, namely the mechanical support from current collectors and the doping of cobalt ions. It can be concluded from this table that the cycling stability of Co^{2+}/Co^{3+}-doped $Ni(OH)_2$ prepared in our work is in the high rank. However, the $Ni(OH)_2$-based materials prepared in a few works [22, 30, 31] show the higher cycling stability than our work. It should be pointed out that the specific capacity of these materials is lower than that of the Co^{2+}/Co^{3+}-doped $Ni(OH)_2$ in this work.

Herein, we attribute the excellent high-rate capacity and high cycling stability of Co^{2+}/Co^{3+}-doped $Ni(OH)_2$ to its two synergistic effects: (1) the structural stabilization by its doped cobalt ions and (2) the mechanical stabilization by its self-supportive structure. It is known that the high-rate capacity of FSs electrode materials depends on their fast transfer of electrolyte ions including the ions diffusion in solid and the ions transportation into/out of the pores in materials. Obviously, the branched nanosheets-interlaced structure in this work satisfies these requirements. It is worth noticing that the stability of electrode materials also significantly affects their high-rate capacity. The structure collapse of materials during the charge–discharge cycles hinders the ions transfer, thus resulting in their poor high-rate capacity and low cycling stability. $Ni(OH)_2$ is an electrochemically unstable material, which requires multiple methods to enhance its stability. In this work, the Co^{2+}/Co^{3+}-doped $Ni(OH)_2$ achieves high stability by the synergistic combination of cobalt ions doping and self-supportive structure, which are the origin of its excellent high-rate capacity.

To further confirm the advantages of Co^{2+}/Co^{3+}-doped $Ni(OH)_2$, we used the Co^{2+}/Co^{3+}-doped $Ni_3(NO_3)_2(OH)_4$ and activated carbon (AC), respectively, as positive and negative electrode materials to assemble asymmetric supercapacitors (ASCs). In Fig. 6a, the CV curves of Co^{2+}/Co^{3+}-doped $Ni(OH)_2$

Table 2 Cycling stability of various cobalt ions-doped $Ni(OH)_2$ in recent typical works

Materials	Electrolyte	Potential window (V)	Capacitance retention	References
Ni-Co LDH/ Ni foam	3 M KOH	0–0.45	98% (3000) at 10 A g^{-1}	[1]
α-β-$Ni_{1-x}Co_x(OH)_2$/carbon nanofiber	6 M KOH	0–0.45	91% (1200) at 100 mV s^{-1}	[19]
Ni-Co LDH honeycomb-like nanostructure	6 M KOH	0–0.5	92% (10,000) at 10 A g^{-1}	[22]
Ni–Co LDH/carbon nanorods and graphene nanoribbons	2 M KOH	0–0.4	83% (2000) at 5 A g^{-1}	[29]
Co–Ni LDH/CFP	1 M KOH	0–0.4	80% (10,000) at 2 A g^{-1}	[30]
Ni-Co LDH hydrangea-like nanostructure	2 M KOH	0–0.5	80% (10,000) at 10 A g^{-1}	[31]
Ni-Co LDH NF	6 M KOH	0–0.6	70% (10,000) at 10 A g^{-1}	[32]
Ni-Co LDH flower-like nanostructure	3 M KOH	0–0.5	79% (2000) at 4 A g^{-1}	[33]
α-$Ni(OH)_2$ /$Co(OH)_2$/GO	6 M KOH	0–0.35	84% (1000) at 5 A g^{-1}	[34]
Ni-Co–OH@ graphene	1 M KOH	0–0.5	66.67% (1000) at 20 mA cm^{-1}	[35]
CBC-N@ Ni-Co LDH	2 M KOH	0–0.4	74.4% (5000) at 100 mVs^{-1}	[36]
$Ni(OH)_2$-$Co_2(OH)_3Cl$// Ni foam	3 M KOH	0–0.5	79% (5000) at 10 A g^{-1}	[37]
$Co_{0.2}Ni_{0.8}$ LDH	6 M KOH	0–0.4	80% (1000) at 10 A g^{-1}	[38]
Co^{2+}/Co^{3+}-doped $Ni(OH)_2$ branched nanosheets-interlaced structure	3 M KOH	0–0.44	82% (7000) at 10 A g^{-1}	This work

and AC measured in three-electrode configuration within potential range of -1.0–0.6 V present their individual characteristic electrochemical properties of electric double-layer capacitors (EDLCs) and FSs [39]. As a result, the CV curves of ASCs at different scan rates within the potential range of 0–1.6 V in Fig. 6b indicate that the ASCs show the combined contribution of electric double-layer capacitance and faradaic capacity. In the GCD curves of Fig. 6c, the ASCs at different current densities present a nearly symmetrical triangular shape and a long discharge platform, further proving its dependence on the redox reaction for energy storage. In Fig. 6d, the ASCs show high specific capacities of 204.8, 150.6, 116.7, 90.9, 81.8, and 54.4 C g^{-1} at respective current densities of 0.4, 1.5, 3.8, 6.3, 7.6, and 11.4 A g^{-1}. In the Ragone plot of Fig. 6e, the ASCs present both high energy and power densities. It has high energy density of 56.9 Wh kg^{-1} at power density of 378.8 W kg^{-1} and still keeps high energy density of 15.2 Wh kg^{-1} at high power density of 11,363.6 W kg^{-1}. In this figure, we also compare the ASCs with those assembled with cobalt ions-doped $Ni(OH)_2$ in other recently published works. It is shown that the ASCs have a prominent energy storage performance [1, 22, 29, 31, 33, 37, 40]. The cycling stability test result of ASCs in Fig. 6f shows that the capacity of ASCs presents a relatively fast decay until 1000 charge–discharge cycles and then stabilizes during the following cycles, keeping a high retention of 91.8% at 10,000 charge–discharge cycle. This result is quite similar to that of sample Co^{2+}/Co^{3+}-doped $Ni(OH)_2$ shown in Fig. 5f. The trend of capacity decay can be attributed to two factors: (1) the falling off of material from electrode due to the weak adhesion of some material particles to current collectors and (2) the structural damage of material because of the stress originating from the volumetric swell and shrink of material. It is considered that the first factor is the main reason for the capacity decay before 1000 cycles, and the second factor becomes the main reason after 1000 cycles because most of material particles with weak adhesion fall off. Therefore, we can judge from Figs. 5f and 6f that the structural stability of material is high. Herein, it can be concluded from the above results and discussion that the

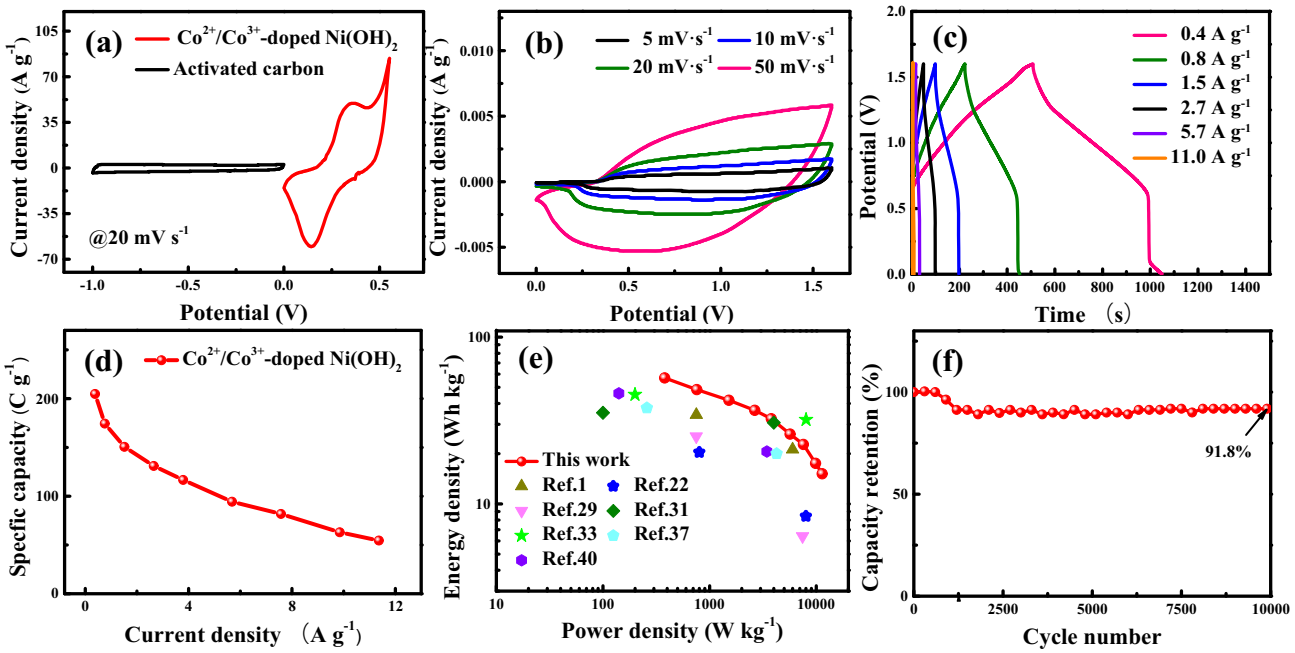

Figure 6 (a) CV curves of Co^{2+}/Co^{3+}-doped $Ni(OH)_2$ and AC at scan rate of 20 mV s^{-1} in three-electrode configuration, (b) CV curves at different scan rates, (c) GCD curves at different current densities, (d) curve of specific capacity vs. current density, (e) Ragone plot, and (f) cycling stability of ASCs at current density of 0.75 A g^{-1}.

Co^{2+}/Co^{3+}-doped $Ni(OH)_2$ with branched nanosheets-interlaced structure is a promising electrode material for high-performance FSs.

Conclusions

In summary, the nanostructured Co^{2+}/Co^{3+}-doped $Ni(OH)_2$ was prepared by a three-step process including synthesis of nanostructured $Ni_3(NO_3)_2(OH)_4$, doping of cobalt ions in $Ni_3(NO_3)_2(OH)_4$, and in situ transformation of $Ni_3(NO_3)_2(OH)_4$ into nanostructured Co^{2+}/Co^{3+}-doped $Ni(OH)_2$. During the synthesis, the branched nanosheets-interlaced structure of $Ni_3(NO_3)_2(OH)_4$ had been kept, finally forming the Co^{2+}/Co^{3+}-doped $Ni(OH)_2$ with structure of same type. Due to the cobalt ions doping and self-supportive structure, the as-prepared Co^{2+}/Co^{3+}-doped $Ni(OH)_2$ presented excellent high-rate capacity and high cycling stability. The as-assembled ASCs also showed both high energy and power density. Based on these results, we believe that the synergistic combination of cobalt ions doping and self-supportive structure is an effective strategy for obtaining $Ni(OH)_2$-based FSs electrode materials with high performance.

Acknowledgement

The authors acknowledge the financial support from Major Scientific and Technological Innovation Project of Shandong Province (No. 2019JZZY010908), Natural Science Foundation of Shandong Province (No. ZR2019MEM036), Key Research and Development Program of Shandong Province (No. 2019GGX103006), and Yantai Science and Technology Project (No. 2019XDHZ088).

Compliance with ethical standards

Conflict of interest The authors declare that they have no conflict of interest.

Electronic supplementary material: The online version of this article (https://doi.org/10.1007/s10853-020-05446-0) contains supplementary material, which is available to authorized users.

References

[1] Liu L, Hou Y, Gao Y, Yang N, Liu J, Wang X (2019) Co doped α-$Ni(OH)_2$ multiple-dimensional structure electrode material. Electrochim Acta 295:340–346

[2] Cao J, Li J, Li L, Zhang Y, Cai D, Chen D, Han W (2019) Mn-Doped Ni/Co LDH Nanosheets Grown on the Natural N-Dispersed PANI-Derived Porous Carbon Template for a Flexible Asymmetric Supercapacitor. ACS Sustainable Chem Eng 7:10699–10707

[3] Su Y, Wu C, Song Y, Li Y, Guo Y, Xu S (2019) Sulfides/3D reduced graphene oxide composite with a large specific surface area for high-performance all-solid-state pseudocapacitors. Appl Surf Sci 488:134–141

[4] Zhao L, Zhang P, Zhang Y, Zhang Z, Yang L, Chen Z (2020) Facile synthesis of hierarchical Ni_3Se_2 nanodendrite arrays for supercapacitors. J Mater Sci Technol 54:69–76

[5] Ruan Y, Wang C, Jiang J (2016) Nanostructured Ni compounds as electrode materials towards high-performance electrochemical capacitors. J Mater Chem A 4:14509–14538

[6] Li B, Zheng M, Xue H, Pang H (2016) High performance electrochemical capacitor materials focusing on nickel based materials. Inorg Chem Frontiers 3:175–202

[7] Yu Z, Tetard L, Zhai L, Thomas J (2015) Supercapacitor electrode materials: nanostructures from 0 to 3 dimensions. Energy Environ Sci 8:702–730

[8] Liu F, Chu X, Zhang H, Zhang B, Su H, Jin L, Wang Z, Huang H, Yang W (2018) Synthesis of self-assembly 3D porous $Ni(OH)_2$ with high capacitance for hybrid supercapacitors. Electrochim Acta 269:102–110

[9] Hall DS, Lockwood DJ, Bock C, MacDougall BR (2015) Nickel hydroxides and related materials: a review of their structures, synthesis and properties. Proc R Soc A 471:20140792

[10] Villars P (2016) $Ni(OH)_2$ ($Ni[OH]_2$) Crystal Structure, PAULING FILE. In: Inorganic solid phases. SpringerMaterials (online database). Springer, Heidelberg. https://materials.springer.com/isp/crystallographic/docs/sd_0558553

[11] Villars P (2016) γ-NiOOH (NiO[OH] rhom) Crystal Structure, PAULING FILE. In: Inorganic solid phases. SpringerMaterials (online database). Springer, Heidelberg. https://materials.springer.com/isp/crystallographic/docs/sd_1703913

[12] Simon P, Gogotsi Y (2008) Materials for electrochemical capacitors. Nat Mater 7:845–854

[13] Huang T, Jiang Y, Shen G, Chen D (2020) Recent Advances of Two-Dimensional Nanomaterials for Electrochemical Capacitors. Chemsuschem 13:1093–1113

[14] Zhou S, Cui S, WeiW CW, Mi L (2018) Development of high-utilization honeycomb-like α-$Ni(OH)_2$ for asymmetric

supercapacitors with excellent capacitance. RSC Adv 8:37129–37135

[15] Kang KN, Kim IH, Ramadoss A, Kim SI, Yoon JC, Jang JH (2018) Ultrathin nickel hydroxide on carbon coated 3D-porous copper structures for high performance supercapacitors. Phys Chem Chem Phys 20:719–727

[16] Xiong X, Ding D, Chen D, Waller G, Bu Y, Wang Z, Liu M (2015) Three-dimensional ultrathin $Ni(OH)_2$ nanosheets grown on nickel foam for high-performance supercapacitors. Nano Energy 11:154–161

[17] Liang J, Jiang C, Wu W (2019) Toward fiber-, paper-, and foam-based flexible solid-state supercapacitors: electrode materials and device designs. Nanoscale 11:7041–7061

[18] Alhebshi NA, Rakhi RB, Alshareef HN (2013) Conformal coating of $Ni(OH)_2$ nanoflakes on carbon fibers by chemical bath deposition for efficient supercapacitor electrodes. J Mater Chem A 1:14897–14903

[19] Huang M, Xu Z, Hou C, Wang S, Zhuang Y, Jia H, Guan M (2019) Intermediate phase α-β-$Ni_{1-x}Co_x(OH)_2$/carbon nanofiber hybrid material for high-performance nickel-zinc battery. Electrochim Acta 298:127–133

[20] Lee JH, Lee HJ, Lim SY, Chae KH, Park SH, Chung KY, Deniz E, Choi JW (2017) Stabilized Octahedral Frameworks in Layered Double Hydroxides by Solid-Solution Mixing of Transition Metals. Adv Funct Mater 27:1605225

[21] Wang J, Li J, Wang M, Liu Y, Cui H (2020) A branched nanosheet-interlaced structure of high performance $Ni(OH)_2$ derived from the isostructural $Ni_3(NO_3)_2(OH)_4$ to clarify the role of structure self-supporting in cycling stability. Sust Energy Fuels 4:1780–1788

[22] Huang B, Wang W, Pu T, Li J, Zhu J, ZhaoC XL, Chen L (2018) Two-dimensional porous (Co, Ni)-based monometallic hydroxides and bimetallic layered double hydroxides thin sheets with honeycomb-like nanostructure as positive electrode for high-performance hybrid supercapacitors. J Colloid Interface Sci 532:630–640

[23] Dong T, ZhangX LM, Wang P, Yang P (2018) Hierarchical flower-like Ni–Co layered double hydroxide nanostructures: synthesis and super performance. Inorg Chem Frontiers 5:3033–3041

[24] Liu Y, Teng X, MiY CZ (2017) A new architecture design of Ni–Co LDH-based pseudocapacitors. J Mater Chem A 5:24407–24415

[25] Cui H, Zayat M, Levy D (2007) Exfoliation-free nanosheet synthesis of transition-metal hydroxynitrate and its transformation to oxide particulate nanosheet. Chem Lett 36:144–145

[26] Tao Y, Li R, Yang T, Li Z (2015) Nickel/cobalt layered double hydroxide hollow microspheres with hydrangea-like morphology for high-performance supercapacitors. Electrochim Acta 152:530–537

[27] Gu J, Sun L, ZhangY ZQ, Li X, Si H, Shi Y, Sun C, Gong Y, Zhang Y (2020) MOF-derived Ni-doped CoP@C grown on CNTs for high-performance supercapacitors. Chem Eng J 385:123454

[28] Rajamathi M, Kamath PV (1998) On the relationship between α-nickel hydroxide and the basic salts of nickel. J Power Sources 70:118–121

[29] Jin H, Yuan D, Zhu S, Zhu X, Zhu J (2018) Ni-Co layered double hydroxide on carbon nanorods and graphene nanoribbons derived from MOFs for supercapacitors. Dalton Trans 47:8706–8715

[30] Wang H, Yang H, Wang D, Cheng D, Deng T, Liu H, Zhang H, Zhang W, Zheng W (2019) Designing chemical bonds between active materials and current collectors for packaging a high-performance supercapacitor. Nanotechnology 31:105402

[31] Wei W, Ye W, Wang J, Huang C, Xiong JB, Qiao H, Cui S, Chen W, Mi L, Yan P (2019) Hydrangea-like alpha-$Ni_{1/3}Co_{2/3}(OH)_2$ Reinforced by Ethyl Carbamate "Rivet" for All-Solid-State Supercapacitors with Outstanding Comprehensive Performance. ACS Appl Mater Interfaces 11:32269–32281

[32] Zhang L, Hui KN, Hui KL, Lee H (2016) High-performance hybrid supercapacitor with 3D hierarchical porous flower-like layered double hydroxide grown on nickel foam as binder-free electrode. J Power Sources 318:76–85

[33] Cao J, Mei Q, Wu R, Wang W (2019) Flower-like nickel–cobalt layered hydroxide nanostructures for super long-life asymmetrical supercapacitors. Electrochim Acta 321:134711

[34] Lai H, Lin L, Lin J, Hsu YK (2018) All binder-free electrophoresis deposition synthesis of nickel cobalt hydroxide/ultraphene and activated carbon electrodes for asymmetric supercapacitors. Electrochim Acta 273:115–126

[35] Lai F, Miao YE, Zuo L, LuH HY, Liu T (2016) Biomass-Derived Nitrogen-Doped Carbon Nanofiber Network: A Facile Template for Decoration of Ultrathin Nickel-Cobalt Layered Double Hydroxide Nanosheets as High-Performance Asymmetric Supercapacitor Electrode. Small 12:3235–3244

[36] Lei X, Shi Z, Wang X, Wang T, Ai J, Shi P, Xue R, Guo H, Yang W (2018) Solvothermal synthesis of pompon-like nickel-cobalt hydroxide/graphene oxide composite for high-performance supercapacitor application. Colloids Surf A 549:76–85

[37] Zhang Z, Du W, Ren X, Shen Z, FanX WS, Wei C, Cao Z, Zhang B (2019) $Ni(OH)_2$-$Co_2(OH)_3Cl$ bilayer nanocomposites supported by Ni foams for binder-free electrodes of

high-performance hybrid supercapacitors. Appl Surf Sci 469:624–633

[38] Meng X, Feng M, Zhang H, Ma Z, Zhang C (2017) Solvothermal synthesis of cobalt/nickel layered double hydroxides for energy storage devices. J Alloy Compd 695:3522–3529

[39] Dubal DP, Ayyad O, Ruiz V, Gomez-Romero P (2015) Hybrid energy storage: the merging of battery and supercapacitor chemistries. Chem Soc Rev 44:1777–1790

[40] Shi D, Zhang L, Zhang N, Zhang Y, Yu Z, Gong H (2018) Boosted electrochemical properties from the surface engineering of ultrathin interlaced Ni(OH)$_2$ nanosheets with Co(OH)2 quantum dot modification. Nanoscale 10:10554–10563

Publisher's Note Springer Nature remains neutral with regard to jurisdictional claims in published maps and institutional affiliations.